Oceanic seismotectonics from regional earthquake recordings: the 4-5N Mid-Atlantic Ridge

DOI:
10.1016/j.tecto.2021.229063

Oceanic seismotectonics from regional earthquake recordings: the 4-5˚N Mid-Atlantic Ridge

Guilherme W. S. de Melo[1,2], Neil C. Mitchell[3], Jiri Zahradnik[4], Fábio Dias[5], Aderson F. do Nascimento[6]

1-Department of Geological Sciences, San Diego State University, San Diego, USA.

2-Scripps Institution of Oceanography, University of California San Diego, San Diego, USA.

3-Departament of Earth and Environmental Sciences, University of Manchester, Manchester, United Kingdom.

4-Department of Geophysics, Charles University, Prague, Czech Republic

5-Observatório Nacional, Rio de Janeiro, Brazil.

6-Departamento de Geofísica, Federal University of Rio Grande do Norte, Natal, Brazil.

This is the green open-access version of the above article accepted for publication in Tectonophysics on 13 September 2021. DOI:10.1016/j.tecto.2021.229063. Link to article:https://doi.org/10.1016/j.tecto.2021.229063.

Highlights

- Regional broad-band seismic records are used to locate earthquakes with small relative uncertainties.
- Results for one swarm show events distributed on multiple faults across rift valley.
- We estimate earthquake depths using water surface reflection and direct P-wave arrival times.
- Shallow earthquake depths derived from surface waveform modeling in the area are estimated to be between 5 and 8 km below seabed.

Abstract

Uncertainties in epicentral locations and hypocentral depths often prevent earthquakes from being associated with individual or group of faults in bathymetric data, thus limiting the understanding of tectonic behavior. Ocean bottom seismometers (OBSs) can overcome this problem, but they take significant efforts to build and deploy, so information from them covers only a minor part of the earthquake record of mid-ocean ridges. As an alternative, a combination of records from seismometers at regional distances and appropriate processing methods can yield location and depth estimates that are useful because they provide extensive data. We illustrate this with a study of of magnitudethe seismicity of the 4-5˚N Mid-Atlantic Ridge using data from seismometers in Brazil, Cape Verdes, and Africa coast. The seismicity occurred in swarms in 2012 (seven events), 2014 (five events), 2016 (62 events), and 2019 (eight events). We compare the seismicity with features in bathymetric data collected with a multibeam sonars, which reveal two detachment fault surfaces ("megamullions"), one close to the modern rift valley floor but offset by ~10 km from it. The located seismicity is shallow (best estimate less than 8 km below seafloor). The swarms occurred over two segments of the ridge and, in the 2016 case, clearly involved movements on widely distributed multiple faults, including faults on both sides of the valley. Although the methods used produce epicenters and hypocenters with uncertainties that are still larger than those of OBS experiments, they could provide a way to study whether seismicity is systematically deep in certain parts of the ridge where megamullions are observed.

Key words: Earthquake, Mid-Atlantic Ridge, Seismotectonics, Waveform Modelling, Seismic Swarms, Detachment Faults

1.0. Introduction

Earthquake seismology has contributed to our knowledge of the tectonics of slow-spreading mid-ocean ridges (MORs) for many decades since it revealed that normal focal mechanisms occur in the median valleys (Sykes, 1967; Thatcher and Hill, 1995; Solomon et al., 1988) and strike-slip mechanisms occur in or near transform faults (Sykes, 1967; Engeln et al., 1986; Wolfe et al., 1993). Associating earthquakes with individual or groups of faults necessary for finer-scale seismotectonic analysis (Scholz, 2002) has relied on the deployment of ocean bottom seismometers (Cessaro and Hussong, 1986; Toomey et al., 1995; Barclay et al., 2001; Grevemeyer et al., 2013; Parnell-Turner et al., 2017; Parnell-Turner et al., 2020). Unfortunately, such deployments have been limited spatially and temporally due to their cost, logistics, and availability of suitable equipment. In addition, data from ocean bottom seismometers (OBSs) also poorly constrain earthquakes located outside their deployed arrays (e.g., Grevemeyer et al., 2013).

Land seismometers and space geodesy allow seismotectonic studies on parts of the ridge system lying above sea-level (Einarsson, 1991) and the Afar depression (e.g., Wright et al., 2006). However, tectonic activity in those areas of thickened crust may not represent that of MORs lying at typical ~2700 m depths. In particular, slow-spreading ridges have low-angle detachment faults (Escartín et al., 2008) described further below, which are not observed in Iceland. Similar comments of unsuitability can be said of other spreading centers surrounded by land stations despite their suitable configurations for locating events, such as the Terceira Rift of the Azores (Vogt and Jung, 2004), as it lies on an oceanic plateau, or the Gulf of California rifts

(Castro et al., 2017), which are highly oblique and sediment-covered. The use of hydroacoustic sensors to locate seismic events from long-distance T-waves has provided greater coverage of the Mid-Atlantic Ridge (MAR) spatially and towards lower earthquake magnitudes (Smith et al., 2002; 2003; Goslin et al., 2005; Simão et al., 2010; Smith et al., 2012b). However, such deployments are unable to provide hypocentral depths and focal mechanisms. Surface waves of earthquakes with moderate (> 5.0 Mw) magnitudes (Cleveland and Ammon, 2013; Cleveland et al., 2018; Howe et al., 2019) from land-based broadband seismometers at regional distances can potentially provide both epicenters and hypocenter of events, and hypocenters of oceanic seismicity. Due to uncertainties in global seismic velocity structure, such data do not allow events associated with individual faults, which are spaced only by ~1-10 km at MORs (Cowie, 1998). However, as we will show below, they are accurate enough to resolve the spatial extent of seismicity, thus revealing the degree to which multiple faults move during earthquake swarms. Additionally, land-based sensors also allow hypocentral depths of the larger events to be determined.

Tectonic spreading (that is not occurring by the intrusion of dikes or other magmatic bodies) was previously thought to involve mainly steeply dipping faults (MacDonald et al., 1977; Shaw, 1992; Shaw and Lin., 1993; Thatcher and Hill, 1995), but the discovery of megamullions (corrugated surfaces believed to have formed by movement on detachment faults) in multibeam sonar data by Cann et al., (1997) led to a rethinking of the underlying mechanism of seafloor spreading. Today geoscientists accept that tectonic spreading occurs by a combination of high-angle and moderate angle faulting, with some detachment faults rotating to low angles to leave megamullions at the seabed (Blackman et al., 1998; Escartin et a., 2003; Smith et al., 2006; Escartin et al., 2008; Smith et al., 2008; Tucholke et al., 2008; Escartin et al., 2016). long-term deployment of OBSs around megamullions by Parnell-Turner et al. (2017, 2020) demonstrated the plethora of information that can be obtained when accurate hypocenters are available. The results showed changes with time in seismicity around one of the detachments, suggesting that the faults undergo stress accumulation and strain release cycles.

Here, we have studied seismicity occurring in three segments of the 4-5ºN MAR where previously collected multibeam and gravity data provide information on the tectonic and crustal structure. The earthquakes (M>3.6) occurred in four swarms. We located their epicenters using waveforms recorded by regional seismographic stations from near the coasts of Brazil, Africa, and the Cape Verde's islands (Figure 1). We used waveform modeling to identify the most likely focal depths of each swarm's strongest events (Mw >5.4). Complementary to previous studies using surface waves recorded by regional networks, we have been able to use delays between water-surface reflected (wpP) and direct arrivals (P) in more distant stations (35˚-95º distance) to constrain hypocentral depths. The swarms appear to be tectonic rather than volcanic and occurred over the inner rift floor of the spreading segments, involving multiple normal faults. Some epicenters were situated on the side of a megamullion closest to the rift center or axis. The hypocenters are sufficiently reliable for us to compare event depths with those from the OBS studies. The study suggests that data from seismic stations at regional (>1,000 km) distances can be used with other geophysical data to study seismotectonic of typical MOR spreading centers.

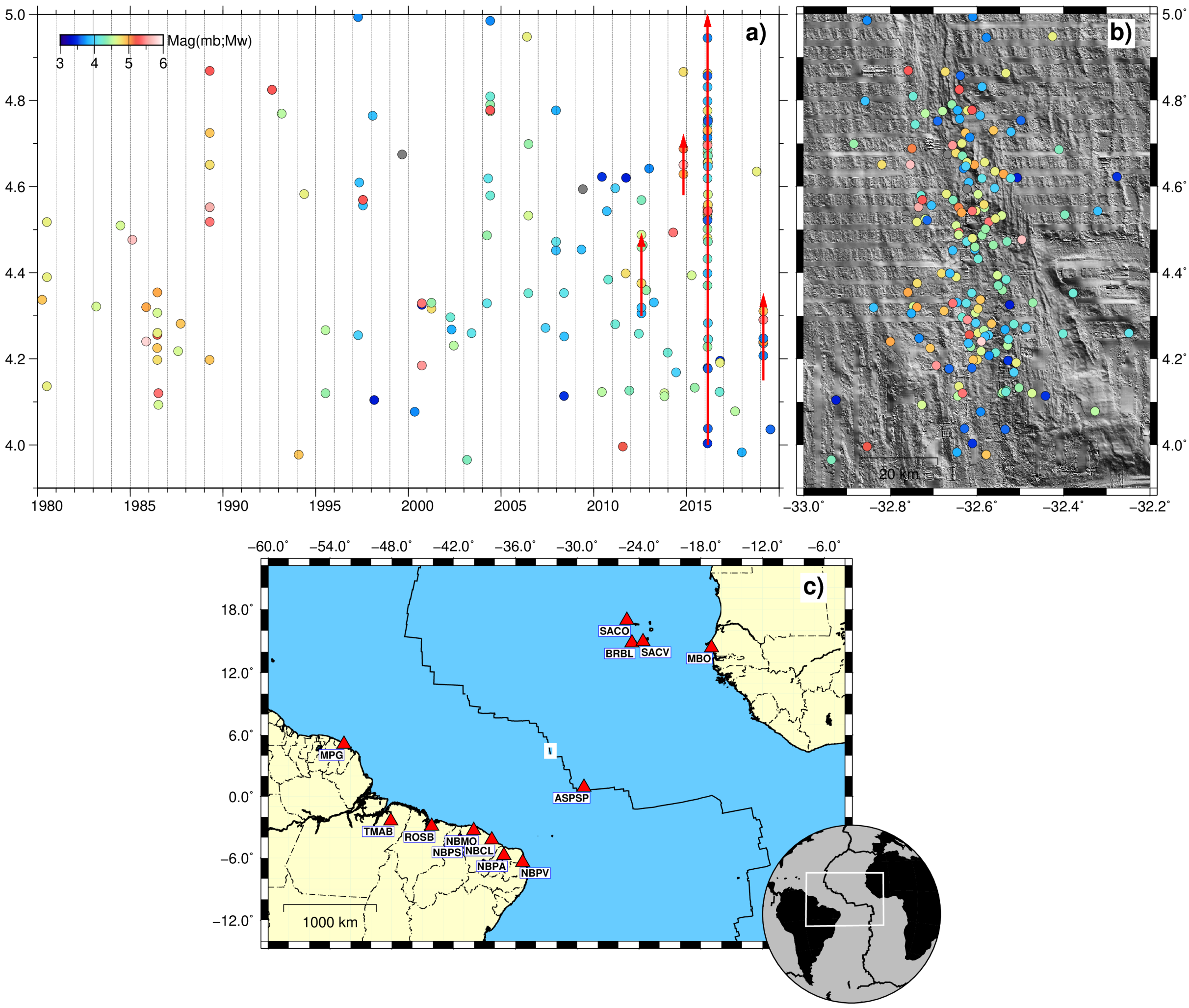

Figure 1 – Distribution of ISC events from 1980 to 2020 along the 4-5ºN ridge segments studied here shown (a) with magnitude and calendar time and (b) map with the epicenters of the ISC coordinates in map of the ISC epicenters overlain on bathymetry (Ryan et al., 2009) shaded from the NE. (c) Locations (red triangles) of the seismic stations used in our study. Small white represents the epicentral area of this study.

2.0. The 4.0º-5.0ºN Mid-Atlantic Ridge

The MAR is slowly spreading with ~25mm/year (DeMets et al., 2010). At 4º-5ºN, it contains three slow-spreading ridge segments (S1-S3 marked in Figure 2a) extending ~100 km north of the Strakhov Transform Valley. Each segment has an axial valley floor at ~3,500 m depth containing a central ridge that we interpret as a neovolcanic ridge. On either side of each valley, the seabed rises to depths shallower than 2,000 m in broad crustal mountains (Figures 2a and 2b). Within the southernmost segment (S3), a major seamount, Nadezhda Seamount, dominates the westerly coastal mountains, rising to 852 m depth (Udintsev et al., 1995). We suspect this feature has a volcanic origin from its shape in profile, elongation along-axis, and some possible NW-SE features on its west side (Udintsev., 1991; Udintsev et al., 1995). In contrast, Muratov Seamount on the east side contains east-west trends on its relatively broad and flat summit ("striations" marked in Figure 2b). We interpret this as a megamullion (M1) produced by a detachment fault (Escartín et al., 2008; Tucholke et al., 2008; Parnell-Turner et al., 2017; 2020). Two out of four rock dredges on the western escarpment E2 of this feature were reported to contain gabbros (Udintsev et al., 1995). A second possible megamullion (M2) lies further north and is separated from the axial valley by a small oblique basin.

Bouguer gravity anomalies broadly support these interpretations. In Figure 2c, two high Bouguer anomalies overlap the suggested megamullion M2 and lie parallel with the Strakhov Transform Valley. Anomalies reach 50 mGal or more above those of the surrounding area to the north, like 30-40 mGal anomaly over the megamullion of the Atlantis Massif (Canales et al., 2004; Blackman et al., 2008). Megamullion M2 is associated with a somewhat smaller deviation of anomalies of ~20-30 mGal, possibly indicating that the crust has been thinned less at this feature than at M1. Nadezhda Seamount, in contrast, is associated with only modest Bouguer anomalies of ~10-20 mGal above those of its surrounding area. This could imply that the seamount has formed by eruption off-axis and that its mass is supported by some plate rigidity, rather than a thickened crust.

We interpret some high-angle normal faults bounding the axial valleys of S1-S3 from the multibeam data. In Figure 2b, a set of faults forming like a flight of stairs bounds the westerly wall (f1w), whereas a more significant flight of faults bounds the easterly wall (f1e). The easterly fault set to their south includes several hook-shaped faults similar to those observed elsewhere (Searle et al., 1998). A prominent west-dipping fault f2e bounds the easterly side of segment S2. To the south-southeast of it, a series of >10 offset faults can be observed lying outside the valley floor. Within segment S3, a broadly curved fault escarpment f3e can be observed, delimiting the easterly side of the valley floor.

Megamullion M2 terminates at escarpment E1, and the high Bouguer anomalies associated with M2 also do not extend west of E1. M2 is, therefore, likely to be inactive. In contrast, megamullion M1 terminates at steep escarpment E2 only 10-15 km from the axis. As fault f3e extends across the westerly side of E2, we suspect that it too is now inactive, or f3e may represent a fault of the megamullion hanging wall and is still active. In that case, the N-S topographic fabric immediately west of E2 overlies a block of original hanging wall material that has or is being uplifted on the footwall.

The study area thus contains some features of interest, which might be tackled with seismological data. Such data could potentially help address questions such as: are megamullions M1 and M2 still active? is there seismicity associated with Nadezhda Seamount? are the high-angle faults active. Additionally, is seismicity on the floor of the MAR typical of tectonic or volcanic swarms? The southern spreading segment abuts a major transform fault: does this lead to deeper seismicity associated with colder lithosphere?

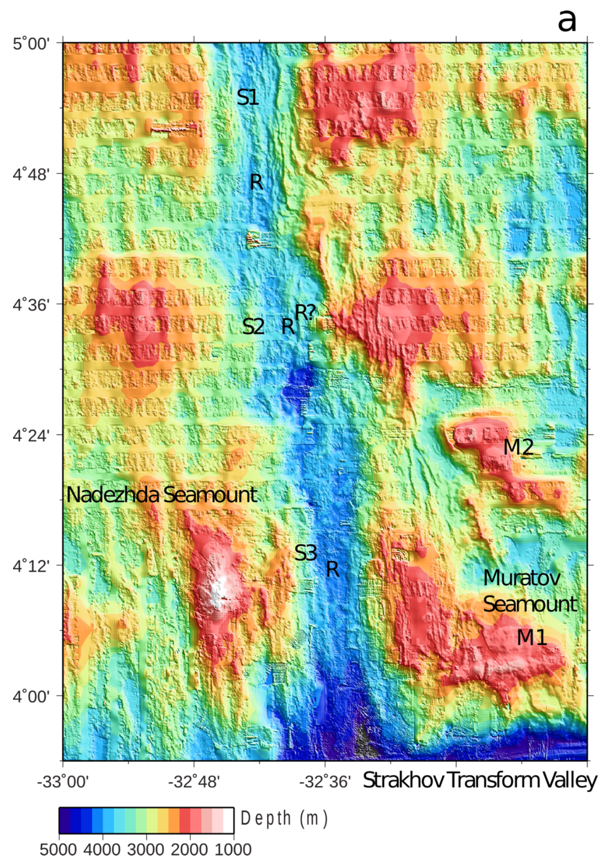
a
5°00'
4°48'
4°36'
4°24'
4°12'
4°00'
S1
R
S2
R
R?
M2
Nadezhda Seamount
S3
R
Muratov
Seamount
M1
-33°00'
-32°48'
-32°36'
Strakhov Transform Valley
Depth (m)
5000 4000 3000 2000 1000

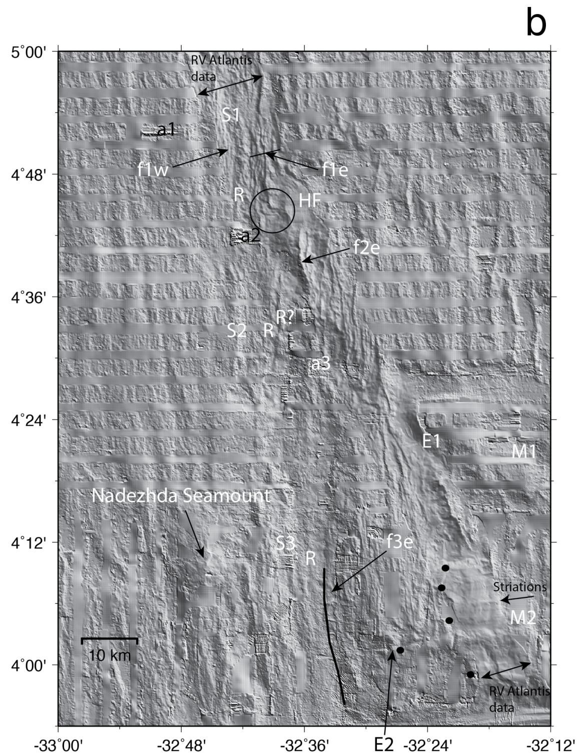
b
5°00'
4°48'
4°36'
4°24'
4°12'
4°00'
RV Atlantis
data
S1
a1
f1w
f1e
R
HF
a2
f2e
S2
R
R?
a3
E1
M1
Nadezhda Seamount
S3
R
f3e
Striations
M2
10 km
RV Atlantis
data
-33°00'
-32°48'
-32°36'
E2
-32°24'
-32°12'

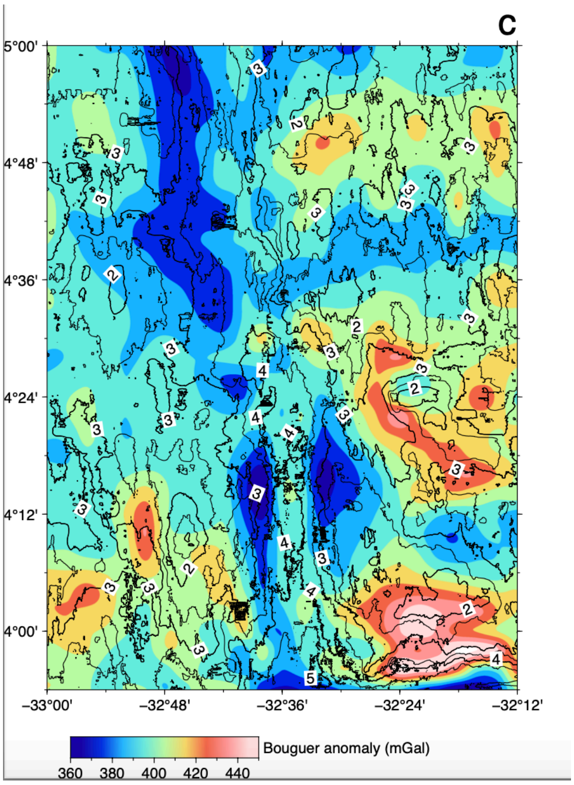

Figure 2 - a) Bathymetry color-coded with annotation a1-a3: multibeam artifacts, S1-S3: spreading segments, R: neovolcanic ridge, M1, M2: megamullion structures, E1, E2: megamullion escarpments, f1w etc.: valley wall faults. Bathymetry data were collected on the RV *Akademic Nikolay Strakhov* in 1988 and 1990 (Udintsev et al., 1995) and by one transit of RV *Atlantis* with a Kongsberg EM122 in 2012 (Parnell-Turner et al., 2012; Smith et al., 2012) running SE to NW across the area. The bathymetry data are the ETOPO1 grid (https://www.ngdc.noaa.gov/, last accessed September 2020). b) As (a) without color-coding. Circle highlights example hook faults. Arrow in SE of map marks the orientations of megamullion stations. Solid circles mark our interpreted limit of those striations towards younger crust. c) Bouguer gravity anomalies from the WGM2012 global model (Balmino et al., 2011; Bonvalot et al., 2012) overlain with bathymetry contours derived from the multibeam data (annotated in km). The Bouguer anomaly version of WGM2012 is a grid in which free-

air anomaly data derived from satellite altimetry were corrected for terrain effects using 2,670 kg/m^3 as the seabed density, and a 1'x1' bathymetry grid (ETOPO1), which includes the RV *Strakhov* bathymetry data. Annotation: NS, Nadejda Seamount and MS, Muratov Seamount (Udintsev et al, 1996).

2.0. Seismological data

The International Seismological Centre (ISC) catalogue contains 181 earthquakes occurring here (4.0º-5.0ºN, 32º-33ºW) from 1980 to 2019 with magnitudes ranging from mb=3.5 to Mw=5.8. Figs. 1a and 1b show the temporal evolution of the ISC events along with their locations. Among these events, 66 of them occurred in four brief swarms on 28 July 2012, 3 November 2014, 20-28 February 2016, and 25 February 2019. A total of 50 focal mechanisms has been provided by the Global Centroid Moment Tensor catalogue for this time interval and area (GCMT, available at https://www.globalcmt.org/, last accessed September 2020). Half of the GCMT solutions occurred during these four swarms, and the four strongest events in these swarms had Mw=5.4 (2012/7/28), Mw=5.5 (2014/11/3), Mw=5.5 (2016/2/21) and Mw=5.5 (2019/2/25).

Figure 1c shows the seismic stations providing the data used in this paper. Since 2011, a broad-band national seismographic network has been operating in Brazil (Rede Sismográfica Brasileira – RSBR, Bianchi et al., 2018). Several regional sources contributed with data for the waveform analysis. These included five Brazilian stations closest to the Atlantic coast (NBPV, NBPA, NBCL, NBMO, ROSB, TMAB), SACV of the IRIS/IDA (Incorporated Research Institutions for Seismology) seismic network (Scripps Institution of Oceanography, 1986) installed in the Cape Verde archipelago and two broad-band stations in French Guiana (MPG) and Senegal (MBO), which are part of the GEOSCOPE global network (Romanowicz et al., 1984). We also used data from two temporary broad-band stations deployed in 2012 on two islands of the Cape Verde archipelago (BRBL and SACO; Faria and Fonseca, 2014). Data from a broad-band station located in St. Peter and St. Paul Archipelago (ASPSP) (de Melo and do Nascimento, 2018) were also used in the epicenter relocation and depth analysis.

4.0.Methodology and analysis

4.1.Epicentral locations

Initially, we reviewed the waveform data from two days before the first event of each swarm until the second day after the last swarm event. We used SCOLV program of the SeiscomP3 package (Hanka et al., 2010) to carry out the analysis. A Butterworth bandpass filter with corner frequencies of 2 and 8 Hz was applied to the waveforms to increase the signal-to-noise ratio (SNR). Then, we used LOCSAT program to locate the epicenters of 24 events not cataloged by the ISC in the 2016 swarm but recorded by the regional stations. The locations were based on the IASP91 velocity model (Kennett and Engdahl, 1991), and the magnitudes of events were estimated to be mb=3.7-4.0. The visual inspection of the seismograms allowed the identification of the Pn waves, though they commonly had amplitudes higher than the recorded noise level. We selected Pn waves for pickings based on the clarity of their onsets for events with mb ≥ 4.5. The maximum time uncertainty of those onsets is ±0.2 s. In contrast, those onsets for the weaker earthquakes (mb<4.5) with lower SNR have uncertainties reaching ±0.5s. Fig.S17 reflects this variation, in which smaller events have greater epicenter location uncertainties.

For the mb<3.9 events absent in the ISC catalogue, locations were found using ISC epicentral coordinates of the strongest events in each swarm, i.e., initial locations during the search. A better SNR was possible in earthquakes with mb=3.8-3.9 recorded by SACV, MBO, NBPV, NBPA, NBCL, NBMO, ROSB, TMAB. ISC events of mb=3.6-3.7 were not readily identifiable in the seismograms due to their low amplitudes relative to background noise. Pn waves for that magnitude range were observed only in the SACV, NBPV, NBPA, NBCL, NBMO, and ROSB records. Earthquakes with mb=4.0-4.4 presented clear Pn and Sn phases in at least the SACV, MBO, NBPV, NBPA, NBCL, NBMO, ROSB, TMAB records.

We relocated the ISC catalogue events and the additional 24 identified by our regional stations using the HYPO71PC plugin of the SeiscomP3 package (Lee and Valdes., 1985). Due to the long distance between the epicentral region and each station, we fixed the depth at 0 km. The location software of Lee and Valdes (1985) also estimates horizontal and vertical location uncertainties. For the horizontal uncertainty, a single radial uncertainty is computed, which is turned into latitude and longitude uncertainties by dividing by the square root of two. As the distribution of recording stations suggests that event longitudes will be better constrained than their latitudes, these uncertainties will over- and under-estimate longitude and latitude uncertainties, respectively. Finally, we computed the epicenter locations using those stations at which the Pn arrivals were interpretable. Relocation employed a 1D velocity model profile extracted from CRUST1.0 for the equatorial Atlantic (Table 1; Laske et al., 2013). Figure 3 shows typical earthquake seismograms.

Depth of layer top (km)	P-wave (km/s)	S-wave (km/s)
0.00	1.89	0.43
0.95	5.00	2.70
1.64	6.50	3.70
3.16	7.10	4.05
7.87	8.11	4.50

Table. 1 – Velocity model used in this study derived from Laske et al. (2013)

4.2.Focal depths

4.2.1.Waveform modeling

Source depths for events of Mw ~5.4 on the MAR were estimated using waveform modeling. Stations on the two sides of the Atlantic are 1,200-2,200 km from the study area, so modeling is well justified in the low-frequency range, e.g., 0.01-0.03 Hz, where many station records have a reasonable signal-to-noise ratio. In this frequency range, it is dominated by the fundamental mode of Rayleigh waves, and simple 1D velocity models may approximate the oceanic crust. Here, we use the model parameters of Table 1 obtained from CRUST1.0.

The modeling was performed using ISOLA (Sokos and Zahradník, 2008, 2013; Zahradník and Sokos, 2018). A causal, fourth order Butterworth filter was used to remove the instrumental responses and to obtain displacement waveforms in the 0.01-0.03 Hz range. We processed the Synthetic displacements with the same filter. Green's functions were calculated using program AXITRA based on a discrete–wavenumber and matrix method (Countant, 1989) implemented in the ISOLA package. We fixed the point-source mechanisms with pure-shear moment tensors using the strike/dip/rake angles taken from the GCMT catalog (Dziewoński et al., 1981; Ekström et al., 2012). Although our tests indicated the possibility of obtaining similar mechanisms (i.e., normal-faulting) as reported in the GCMT for the studied events (Table 2), we identified from deviatoric inversion (Sokos and Zahradník, 2008) that, because the station distribution is not uniform, our own moment-tensor inversion is not optimally conditioned and thus full moment-tensor inversion was not performed. We instead inverted for solutions with pure double-couple focal mechanisms. The centroid position was also fixed horizontally at the GCMT epicenter location. This choice left the vertical position of the centroid unknown, and hence the analysis was used to constrain the depth.

The seismic moment rate of each event was assumed to be a delta function because the source durations of the analyzed events were shorter than the minimum considered period (33 s). The best-fitting solution is described by the optimal depth (or the depth range), scalar moment (Mo), moment magnitude (Mw), and variance reduction VR (<=1). A 95% confidence interval to VR was numerically estimated using an extended frequency range 0.01-0.04 Hz. ISOLA was run for several frequencies and, for each run, solutions were saved with a new focal depth (Dias et al., 2016). A spurious, rapid drop of the correlation between real and synthetic seismograms was identified for trial source depths shallower than 4 km, caused by numerical problems in the Green's functions calculations. Therefore, the inversion was applied using depth trials ranging from 4 until 20 km were performed.

Date	Origin Time	Lat (º)	Long (º)	Mw	Strike (º)	Dip (º)	Rake (º)	DC (%)
2012/7/28	16:01:16.3	4.61	-32.58	5.4	195	45	-79	92
2014/11/3	08:24:00.3	4.86	-32.60	5.5	351	45	-103	93
2016/2/21	01:26:04.6	4.79	-32.56	5.5	360	44	-92	80
2016/2/27	02:41:48.0	4.64	-32.59	5.4	355	44	-99	90
2019/2/25	15:05:35.5	4.30	-32.57	5.5	169	45	-98	94

Table. 2 – GCMT parameters of the earthquakes used in this study (Ekström et al., 2012). In the GCMT analysis, all centroid depths were fixed at 12 km.

4.2.2.Modeling depth-phase wpP

The four strongest events with magnitude Mw > 5.4 were also recorded by some teleseismic stations located in North America, Europe, Middle East, and Africa. In these data, the water surface reflection phase (wpP) was typically well recorded in stations located >30º distance from the epicenters. Focal depths were computed from

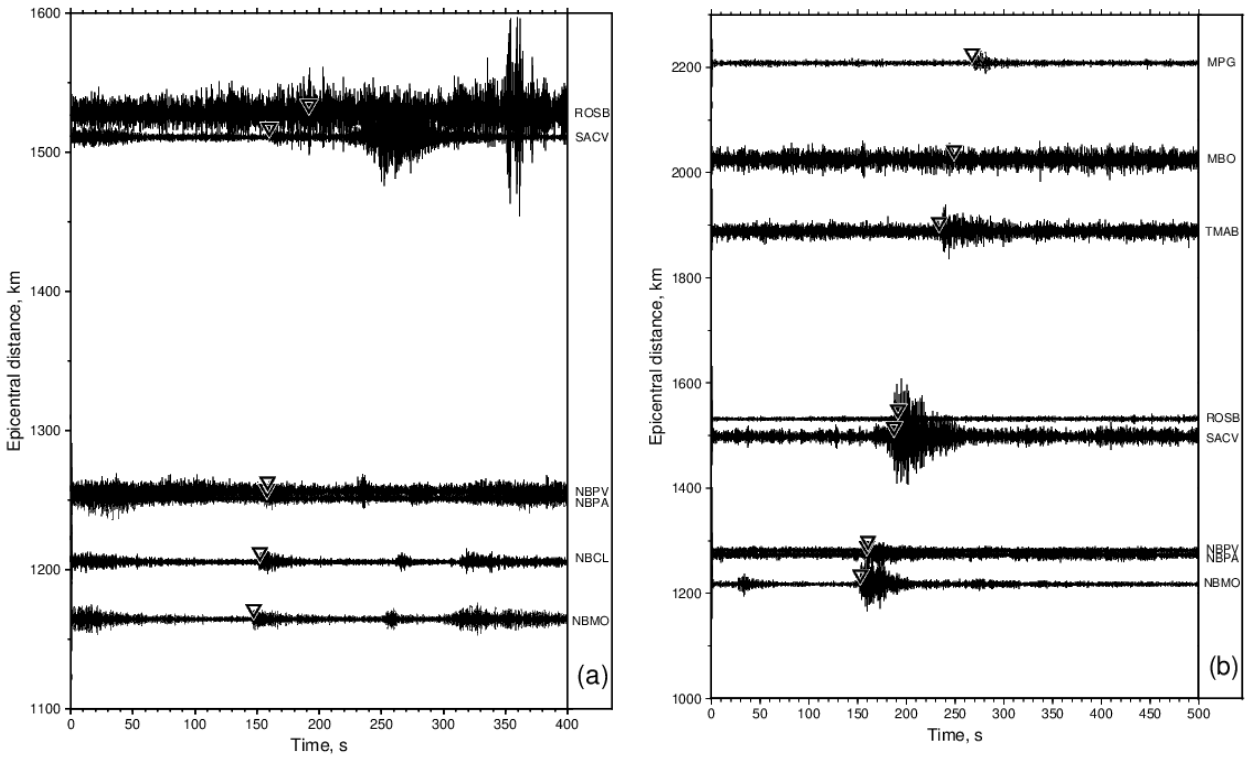

the wpP-P time differences and the P-wave velocity profile (Table 1) using the method of Assumpção (1998) and Assumpção et al. (2011). This involves applying the equation for the time delay $wpP - P = \sum_{j=1}^{n}\left(\frac{2h_i cos i^{\circ}}{V_j}\right)$ where h_i is the thickness of each layer in velocity model, i° the incidence angle of the ray in the layer and $V_j$the P-wave velocity of that layer. The incidence angle is obtained from $i^{\circ} = sin^{-1}\left(\frac{V_j}{V_{ap}}\right)$, in which V_{ap} is the apparent velocity obtained from the pP ray parameter. We used the TauP travel time calculator (Crotwell et al., 1999) to estimate the ray parameter from the IASP91 global model (Kennett & Engdahl., 1991).

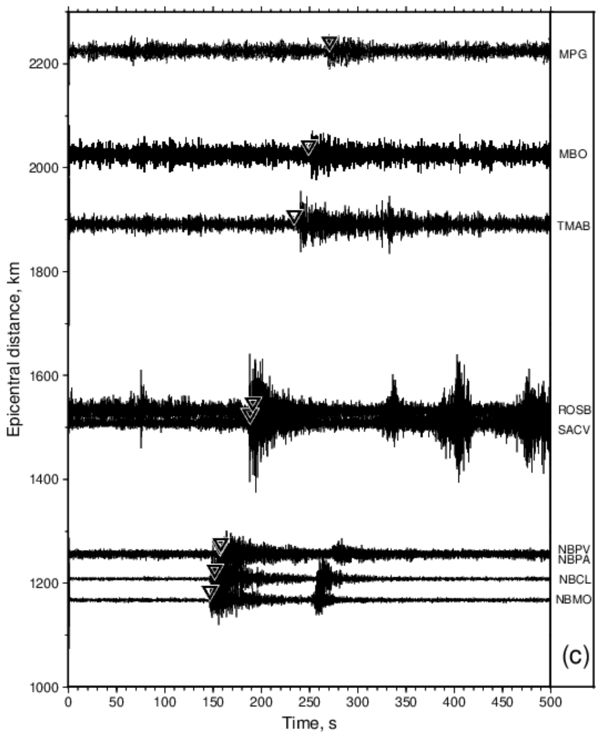

Figure 3 – Typical earthquake waveforms used in this study. Seismograms are plotted with a 4–9 Hz Butterworth filter. (a) Event mb 3.9 of 02/20/2016 at 13:00:58. (b) Earthquake of 11/03/2014 at 06:25:14 and magnitude mb 4.5. (b) One of strongest events of the 2014 swarm, of 02/27/2016 at 02:41:47, Mw 5.4. Inverted triangle marks the identifiable Pn arrival times.

5.0.Results

5.1.Seismicity

5.1.1.The 2012 micro swarm

The 2012 swarm was short with eight ridge axis 4.05º-4.2ºN events (Figure 4; Table S1). The swarm began at 15:20:17 GMT July 28 and ended at 16:18:46 GMT on the same day. Magnitudes ranged from mb 3.7 to Mw 5.4 (Figure 5a). The root-mean-square residual (RMS) was 0.2-0.8s (Figure 5e). The horizontal uncertainties were 1-7 km (Figure 5i), with most of them < 6 km. The relocated epicenters were situated near the ridge-transform intersection (4.05°-4.2ºN, 32.6º-32.5ºW). Two epicenters were located on the inner floor of the median valley (4.18º-4.2ºN), and another six epicenters were in the eastern valley wall (4.05º-4.2ºN).

5.1.2.The 2014 micro swarm

2014 swarm was also of short duration, with only five earthquakes cataloged by the ISC, and situated at 4.7º-4.9ºN in the axis, north of the 2012 events (Figure 4; Table S2). They began at 06:25:09 GMT on November 3 and ended at 08:27:06 GMT on November 3. They had a magnitude range of 4.3-5.4 (Figure 5b). Three events occurred on the inner floor (4.8º-4.9ºN) and the other under the median valley wall (4.7º-4.8ºN). The relocated results had RMS 0.1-0.8s (Figure 5f), and three had RMS <0.2 s. The horizontal uncertainties of the relocations were 1-4 km (Figure 5j).

5.1.3.The 2016 swarm

The 2016 swarm had more events (Figure 4; Table S3), with 62 events recorded over a few days with magnitudes of 3.6-5.5 (Figure 5c). RMS uncertainties were 0.1-1.3s, with 53 of them having <0.6s (Figure 5g). Horizontal location uncertainties were 1-11 km, with 46 earthquakes having <8 km (Figure 5k). The seismicity occurred in two stages and moved over an entire segment of approximately 42 km in length. The first stage with 45 earthquakes started with a mb 3.7 event at 05:00:10 GMT on February 20. The activity continued until 14:19:06 GMT on February 22, and most of the events occurred in the first three hours of February 20. The event frequency then declined gradually (Figure 6a). After five days, an earthquake (02:41:45 GMT on February 27) started the second sequence of 17 events until 18:38:56 GMT on February 28. However, despite the gap between the two stages, one cannot rule out the possibility that the seismicity was continuous, with weak activity between the stages not being detected by the regional stations.

Figure 6b illustrates the spatial-temporal behavior of the 2016 swarm. Initially, on February 20, 32 earthquakes were asymmetrically scattered over a latitude range (4.4-4.8ºN). Most epicenters were situated on the inner floor of the median valley. Eleven events occurred in the west valley wall and another five in the east wall. On February 21, the seismicity was also spatially irregular but comprised only 13 events. On February 27, the epicenters were also distributed asymmetrically in the second swarm stage, but over a seismic zone 25 km in length (4.5-4.68ºN). Five other events occurred on the inner floor of the valley, and more than five events occurred over the east valley wall. The remaining seven seismic events had epicentral solutions off-axis.

5.1.4.The 2019 micro swarm

The 2019 swarm comprised only eight earthquakes over 4.2º-4.35ºN (Figure 4; Table S4). This swarm started at 15:05:09 GMT and ended at 21:10:48 GMT. Magnitudes ranged from 3.6 to 5.5 (Figure 5c). Relocations had RMS errors of 0.1-1.2s, with seven events with <0.3s (Figure 5h). Horizontal uncertainties were 2-8 km (Figure 5i). All epicenters lay outside the media valley floor and around Nadezhda Seamount, with only two events in the median valley wall (right side of Figure 4).

Figure 4 – a) Epicenter locations (color circles) of the earthquakes obtained from ISC catalog and the events cataloged in this study (black square symbols). b) Epicenters relocated using HYPO71 of the SeiscomP3 package. The GCMT focal mechanisms of 5 events (Table 2) are also shown. White circles with red line are epicenters recorded by the OBSs array deployed during the 11th cruise of the RV *Akademik Nikolai Strakhov* in 1988 (Udintsev et al., 1996).

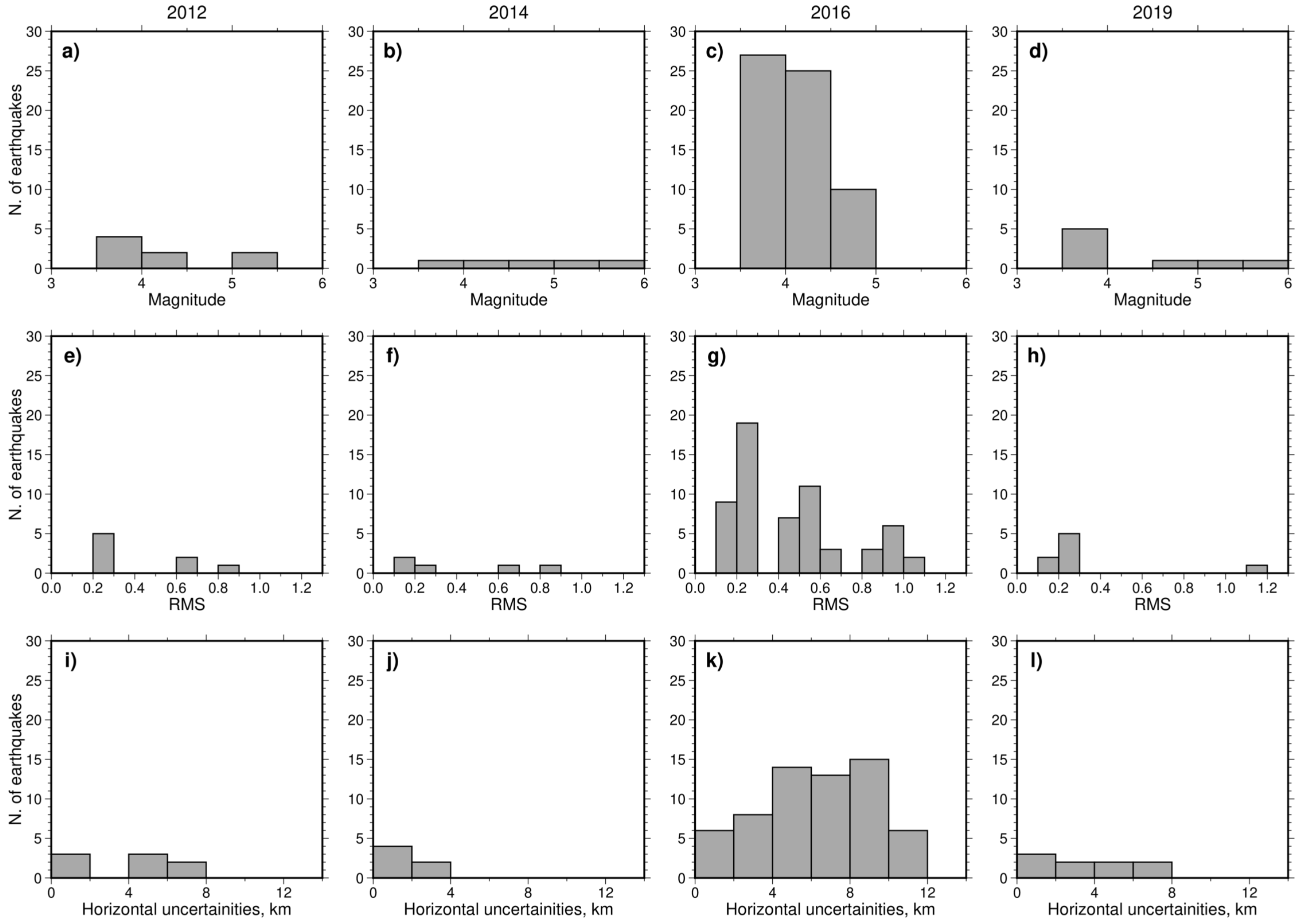

Figure 5 - (a-d) Histograms showing the distribution of magnitudes of the earthquakes from the four swarms. (e-h) RMS residual distribution. (i-l) Horizontal uncertainty distributions.

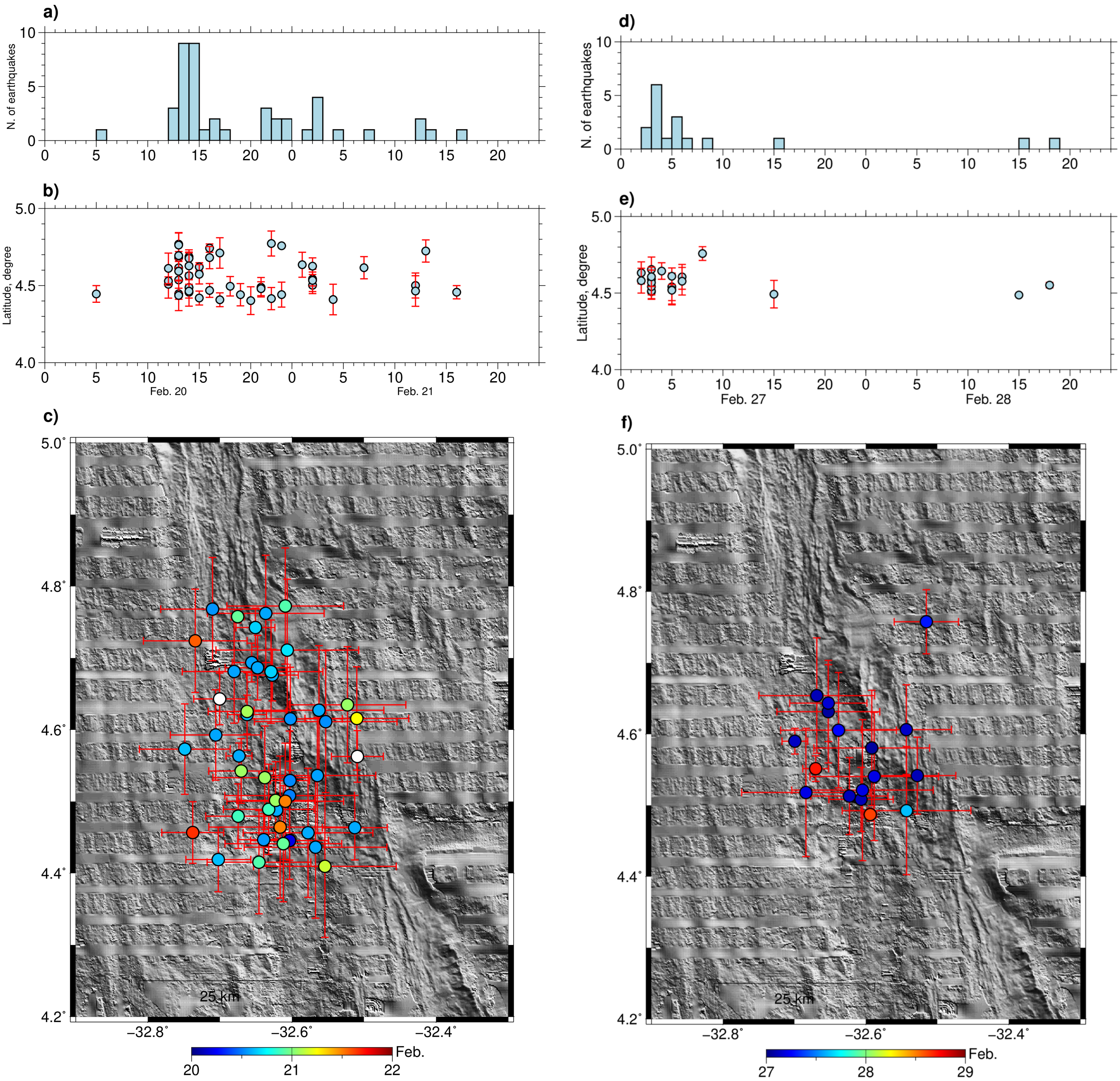

Figure 6 - Temporal development of two 2016 swarms. (a) and (d): event counts. (b) and (e) latitudinal distributions. (c) and (f): plan-view evolutions.

5.2.Focal depths

5.2.1.Surface-wave inversion results

The processing for depths, as detailed in section 4.2.1, was applied to the five large events given in Table 3. The first event (from the 7/28/2012 swarm) occurred at 16:01:22 GMT. It had a relocated epicenter in the eastern valley wall (4.147ºN, 32.520ºW). Using the GCMT strike 192º, dip 45º, and rake -79º, we obtained the best variance solution with a depth of 8 km and centroid time (CT) of +4.8s relative to origin time, with Mo=1.91 x 10^{17} Nm, Mw=5.46, and VR=0.66. Figure S1 illustrates the acceptable waveform fit using the 8 km centroid depth. Figure S2 shows the waveform correlation as a function of trial depth. The complete E-W components from the available stations have a waveform quality with a low signal-to-noise ratio.

Similarly, only the MPG station N-S component was used in the analysis, and parts of the record horizontal components were not used in the inversion. Nonetheless, all vertical components had good quality. The depth obtained is relatively well resolved because the major wave groups, formed by Rayleigh surface waves, are sensitive to the depth.

Date	Origin Time	Lat (º)	Long (º)	Mw	CT	Depth (km)	VR
2012/7/28	16:01:22	4.15	-32.52	5.5	+4.8	8.0	0.66
2014/11/3	08:23:58	4.85	-32.71	5.5	+3.2	7.0	0.65
2016/2/21	01:26:03	4.76	-32.73	5.4	+3.6	6.0	0.67
2016/2/27	02:41:47	4.64	-32.59	5.4	+2.5	5.0	0.71
2019/2/25	15:05:37	4.25	-32.76	5.4	+4.2	5.0	0.68

Table. 3 – Moment magnitudes Mw, centroid times CT and focal depths obtained in this study for the five strongest earthquakes reported by the GCMT. Origin Time, Latitude, and Longitude coordinates reported in this table were obtained from the relocated earthquake catalog. Also shown is variance reduction of the waveform modeling (VR).

The strongest earthquake of the 11/3/2014 swarm (08:23:58 GMT) was relocated (4.848°N, 32.711ºW) in the inner floor of the median valley. The inversion indicated a depth of 7 km and CT of +3.2s, with Mo 2.42 x 10^{17} Nm, Mw 5.52, and VR 0.65. The best waveform fit is shown in Figure S4 and Figure S5. N-S and E-W displacements in the ASPSP and SACV station data were not used for this inversion because of their large noise levels. Instead, all other components of the available stations were applied in the inversion.

For the 2/21/2016 earthquake (01:26:03 GMT), the epicenter was relocated (4.758ºN, 32.730ºW) to the inner floor of the median valley. The inversion resolved a depth of 6 km (VR 0.67, CT +3.6s), with a moment magnitude of 5.43 and Mo 1.76 x 10^{17} Nm. N-S sensor components of SACV, MBO, and MPG stations were not used because of noise. ASPSP station did not record this or later events due to technical and logistic issues. The best model is shown in Figure 7, and all trial depths in Figure S7.

The second strongest event of the 2016 swarm of 2/27/2016 (02:41:47 GMT) was relocated (4.631ºN, 32.652ºW). The inversion resolved a shallower depth of 5 km, with VR 0.71 and centroid time +2.5s, with moment 1.48 x 10^{17} Nm and Mw 5.38. Because of the high noise levels, several sensor components were not used in the inversion (N-S for SACV, MBO, and MPG and E-W for SACV, ROSB, and TMAB). All vertical components were used in the inversion, however. The results of waveform modeling and the trial depths are shown in Figure S9 and Figure S10.

The last event, 2/25/2019 (15:05:37 GMT) was relocated outside the ridge axis in shallower bathymetry (4.254ºN, 32.766ºW). Hypocentral inversion suggested a depth of 5 km and moment-magnitude of 5.42, with Mo 1.76 x 10^{17} Nm, VR 0.68, and CT +4.2s. Due to noise, N-S sensor components were used only from NBMO, NBPV, and ROSB, and E-W components from only ROSB, SACV, TMAB, and MPG. The ROSB vertical component was also not used because of a technical problem with the equipment. The results of the best solution can be observed in Figure S12 and Figure S13.

5.2.2. Depths from wpP-P phases

We derived focal depth for the Mw 5.4 earthquake of 2/27/2016 (02:41:47) using the time difference between the wpP and P phases. We used records from 19 IRIS stations (Table S5), with azimuthal gaps over 130-170º and 230-290º. The stations were chosen where seismograms revealed separate wpP and P phases. Trends with epicentral distance were fitted to downward motions of the first P-phases as shown in Figure 8. The wpP phase can be clearly seen with a large peak ~5.3-5.9s after P. Using the method of section 4.2.2 and our velocity model of Table1, we interpret the observed wpP-P time differences as indicating a hypocenter depth of 5.1±0.1 km, which is close to the depth of 5 km estimated with the ISOLA waveform inversion. From the consistency of the wpP-P time difference among the stations, the depth is well constrained (Figure 9). In Fig. 9, we also compare the result with five hypocenter depths (5, 6, 7, 8, and 9 km) estimated using the theoretical pP-P phases of the IASP91 global velocity model, corrected with a water layer. This approach yields a hypocentral depth of 7 km. We speculate that this ~2-km difference between the estimated wpP-P and IASP91 depth arises because the IASP91 travel time table was derived using events located primarily on the continental crust (Kennett and Engdahl, 1991).

The success of depth estimations from the wpP and P waves leaves open the question of why the bpP phases are so weak. Large amplitudes of water-reflected P waves, wpP, have also been reported also for other phases, as such PKP waves recorded in OBSs (Blackman et al.,1995). Strong reflections have also been inferred for events recorded passing over the South America continental shelf (Assumpção, 1997; Assumpção et al., 2011). Relatively small amplitudes of bpP phases have been explained by the smaller impedance contrast at the seabed than on the ocean surface (Shearer and Orcutt, 1987). We suggest that the effect is even more severe for remote recordings of events originating at the 4-5°N MAR axis because the oceanic basement is exceptionally rugged (Figure 2), leading to scattering and loss of coherence of the basement-reflected P wave.

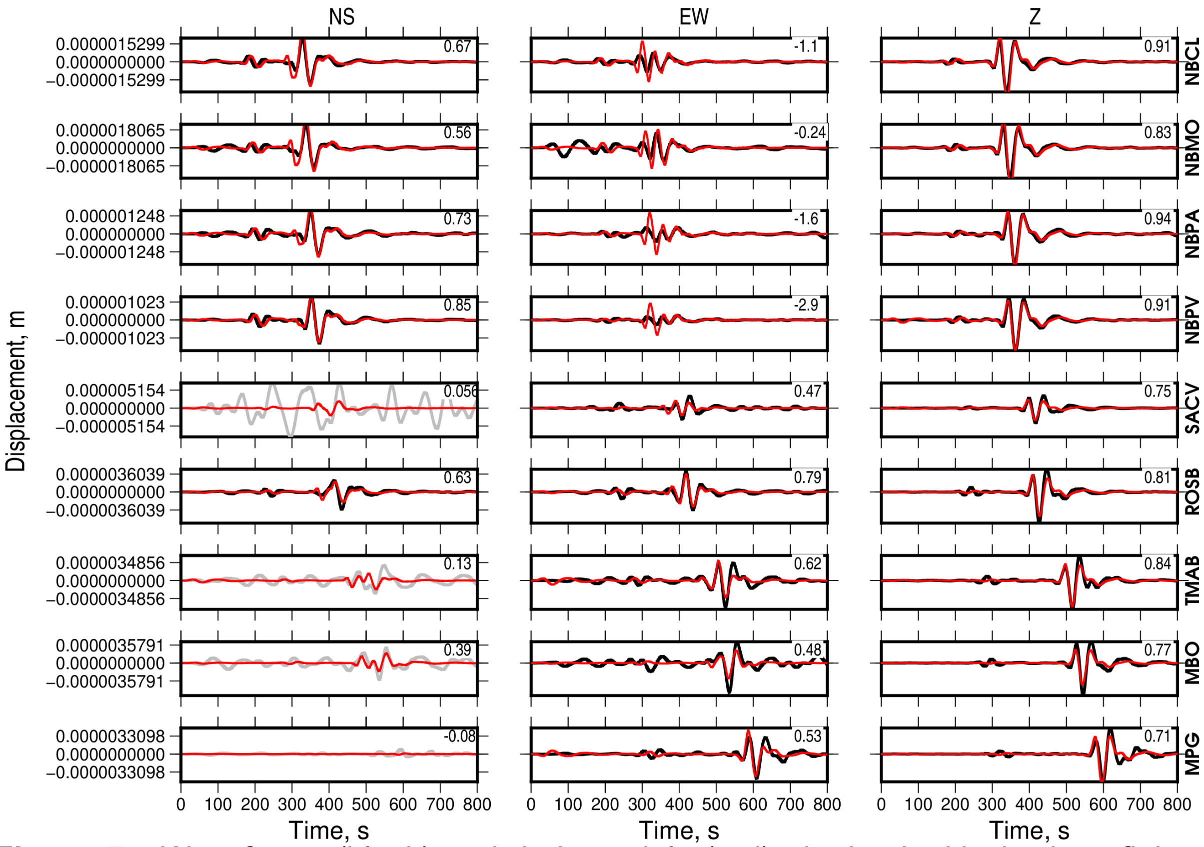

Figure 7 - Waveforms (black) and their models (red) obtained with the best-fitting source position in the 2/21/2016 swarm. The model has a 6-km depth, VR=0.67, fixed GCMT mechanism. Data plotted in gray were not used in the inversion due to noise. Numbers at the top-right corner of each panel are the variance reduction for a particular component.

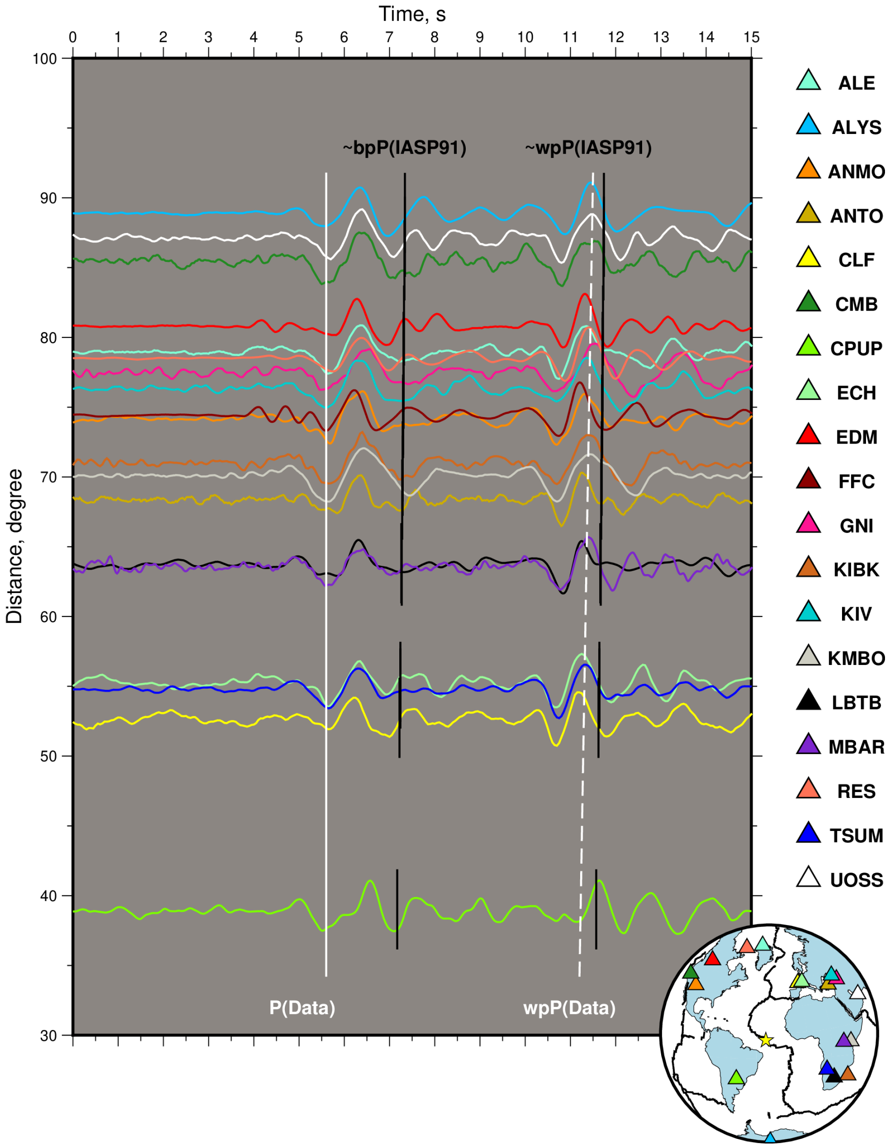

Figure 8 - Example of P and wpP phases on teleseismic records, after removing instrument response from WWSSN short-period instruments for Mw 5.4 strike-slip event on 27 February 2016 (GCMT). Continuous and dashed white line locate the interpreted P and wpP phases. Solid black lines present the theoretical IASP91 bpP phase, and wpP is estimated using the time delay due to the water depth at the epicenter. Seismogram colors present the specific station used in the analysis, with their locations shown in the short spherical globe in the inferior right corner.

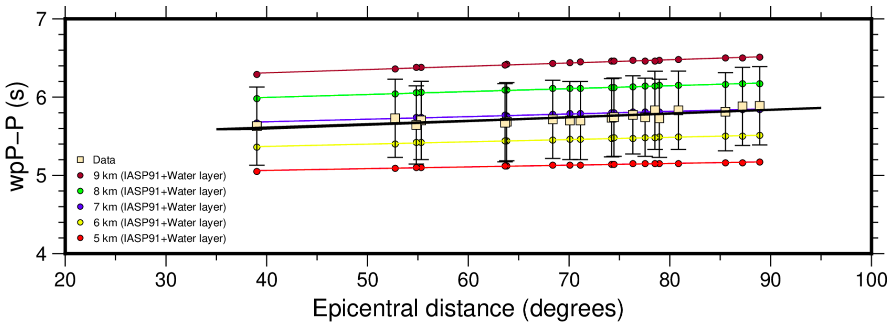

Figure 9 – Fit to the wpP-P time differences read from seismograms shown in Figure 5. Data are shown by squares and vertical bars their uncertainties. The bold line presents the best-fitting trend for the 5.1 km depth. Color circles are theoretical time differences calculated using the IASP91 tables of pP phase for the 5, 6, 7, 8, and 9 km depths, corrected for the water layer.

6.0. Discussion

We compare our results to see if they are compatible with those of other studies and then assess how the methods could be used more effectively to tackle problems of the tectonics of mid-ocean ridges.

6.1. Seismic behavior at the 4º-5ºN ridge axis

Earthquakes have been associated with dike intrusions at MORs, most identified with axial volcanoes. Such intrusions occur less frequently at slow-spreading ridges, where they occur globally on average only every five years (Bohnenstiehl and Dziak, 2009). Over 2000-2010, only two dike intrusions were detected on the MAR, both at the Lucky Strike segment in 2001 and 2010 (Dziak et al., 2004; Giusti et al., 2018). During those intrusions, seismicity occurred over distances of ~55 km in 2001 and ~70 km in 2010 (Dziak et al., 2004; Giusti et al., 2018). Dike intrusions involve seismicity propagating in the direction of intrusion associated with deformation at the dyke tip (Einarsson and Brandsdottir., 1980; Dziak et al., 1995; Dziak and Fox, 1999). Such time progressions were not identified for the 2016 swarm. In contrast, tectonic swarms in the MAR typically occur in a seismogenic zone of mainly extensional deformation that is 10-20 km across-axis, with most epicenters located within the inner median valley (Toomey et al., 1985; Bergman and Solomon, 1990). Bergman and Solomon (1990) also suggest that strong events of magnitude >5.4 frequently occur at the boundary faults of the inner floor of the median valley, with a maximum distance of 10-15 km from the axis of accretion.

Even allowing for the significant epicenter location uncertainties, the 2016 swarm at 4.0º-5.0ºN was spread out over the axial valley, so it was more like a tectonic swarm than a volcanic swarm. Most epicenters were located within the axial valley or at most 15 km from the inner floor of the valley. Similar results with earthquakes occurring over the inner floor and valley wall have been reported by Toomey et al (1988) at the MAR near 23ºN. Klein et al. (1977) suggested that movements on multiple faults can be identified in data from a swarm seismic zone on the Reykjanes Peninsula. The seismicity behavior with the time of the four short swarms could be part of a continuous tectonic cycle, expected from the thermoelastic stress changes caused by rapid cooling (Bergman and Solomon, 1984).

High Gutenberg-Richter b-values can occur in oceanic swarms where a large proportion of microearthquakes are generated by volcanic activity (e.g., on Hawaii and Iceland), with values reaching 2.5 (Lay and Wallace, 1995). However, according to Cessaro and Hussong (1986), smaller b-values are more associated with uniform and high-stress regimes that cause tectonic earthquakes. This may explain the lower b-values of 0.75-1.05 found in swarms of the slow-spreading MAR 0.5º-45ºN (Lilwall et al., 1977; Francis, 1978; Cessaro and Hussong., 1986; Toomey et al., 1988; Kong et al., 1992; Wolfe et al., 1995; Barclay et al., 2001). Figure 10 shows a Guttenberg-Richter graph for the 2016 swarm, suggesting an approximate b-value of 0.88, consistent with a tectonic rather than a volcanic swarm.

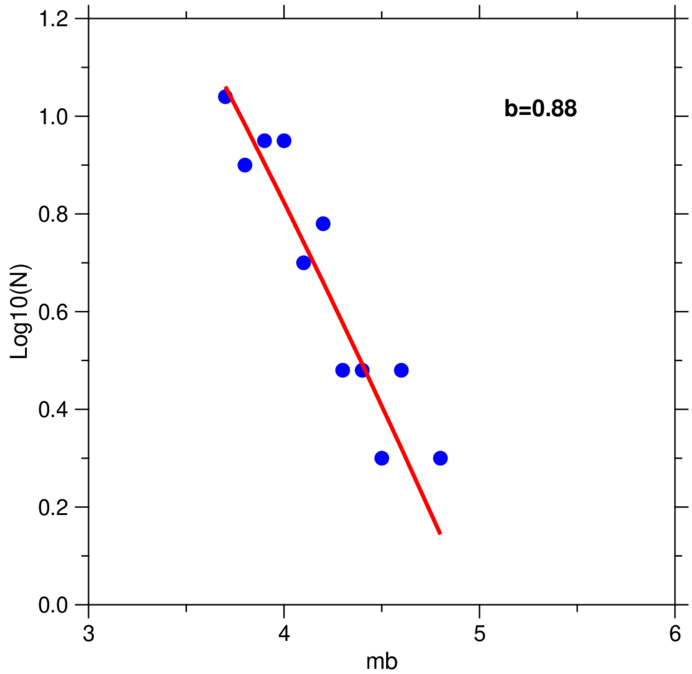

Figure 10 – Gutenberg-Richter graphic of earthquakes from the 2016 swarm. Number of earthquakes for each magnitude are presented in blue circles. The b-value shown is the slope of the best fitting regression (red line).

6.2. Comparing earthquake depth with cross-axis relief

Cross-axis topographic relief is the variation in elevation from the rift valley floor to crestal mountains, which is thought to represent the strength and thickness of the lithosphere underling continuous tectonic necking (Tapponier and Francheteau, 1978). Several authors have observed an apparent correlation between the maximum hypocenter depth with cross-axis relief of the MAR (Kong et al., 1992; Barclay et al., 2001; Tilmann et al., 2004). We have computed similar measures of topographic relief to see if our hypocenter depths are consistent with this correlation. Figure 11 shows hypocenter depths of the four strongest earthquakes analyzed of 2012, 2014, and 2016. In Figure 11, epicenters are shown versus the cross-axis relief along with other measurements from the MAR at 35ºN (Barclay et al., 2001), 29ºN (Wolfe et al., 1995), 26ºN (Kong et al., 1992), 23ºN (Tommey et al., 1988), 17.5ºN (Cleveland et al., 2018), 16.5ºN (Cleveland et al., 2018), 15.5ºN (Cleveland et al., 2018), 13.5ºN (Parnell-Turner et al., 2017), 5ºS (Tilmann et al., 2004), 7.2ºS (Grevemeyer et al., 2013), and

7.8ºS (Grevemeyer et al., 2013). The focal depth results obtained in this work lie within the same graph-space as previous studies and therefore appear consistent with them.

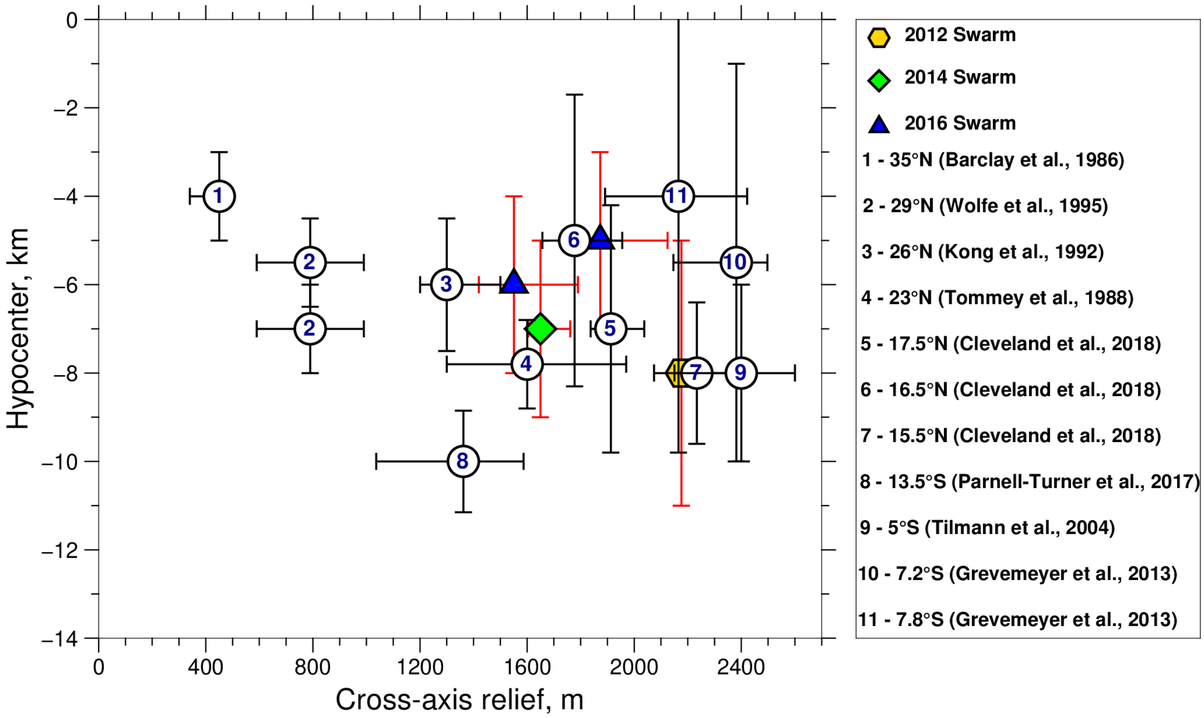

Figure 11 – Relation between cross-axis topographic relief and maximum depth of each swarm, revealing a tendency for the deepest earthquakes to be deeper with increasing relief up to ~1400 m. Cross-axis relief was determined in a manner similar to the earlier studies by averaging the relief from the inner valley floors using bathymetry cross-sections obtained with GeoMapApp software in the vicinity of the earthquake epicenters (method following Barclay et al. (1996)). Data from 35ºN, 29ºN, 26ºN and 23ºN are from Barclay et al. (1996).

The 2012 event occurred at 8±3 km depth and was located in the eastern valley wall near megamullion M1, where there is nearly 2,150-2,200 m of cross-axis relief. Thus, it lies within a similar area to that of deeper events of Cleveland et al (2018) for 15.5ºN. From the hypocenter depth uncertainty bars, the 2012 event also overlaps with the event of 13.5ºN, where seismicity is linked to detachment fault (Craig and Parnell-Turner, 2017; Parnell-Turner et al., 2017). However, that depth does not continue the trend of increasing maximum depth of seismicity with cross-axis relief in Figure 11; rather it is shallower. Parnell-Turner et al. (2020) demonstrated using the microearthquake data recorded in two OBS deployments at 13.2ºN that deformation around detachment faults occurs in cycles, leading to variations in earthquake location over time. Therefore, the shallower maximum depth of the 2012 event could either represent a shallow seismicity stage of a cycle associated with megamullion M1, or alternatively, M1 is no longer active, and the seismicity was due to other, perhaps steeply dipping faults.

6.3. Epicentral and hypocentral uncertainties

To put our study in perspective and consider the potential utility of our methods, we review uncertainties here. Epicenters of mid-ocean ridge earthquakes have varied uncertainties, depending on the method used, data characteristics, distance to instruments, and uncertainties in velocity of the mantle or other intervening medium. for example, epicenters recorded by teleseismic stations can have horizontal location uncertainties ranging from 5 to 50 km (Bergman and Solomon., 1984; Cleveland et al., 2018). In contrast, regional hydrophone networks can record many more earthquakes of lower magnitude with epicenter uncertainties in some cases less than 4 km (Fox et al., 2001; Smith et al., 2004; Goslin et al., 2012; Giusti et al., 2018), but occasionally reaching 75 km (Cleveland et al., 2018). Recordings from OBS arrays can locate epicenters within only 0.9 km (Parnell-Turner et al., 2020), but such data are typically recorded only over a short period (months to a year) for each deployment. Leaving aside the problem of potential bias due to global model velocity errors, the precisions of our epicenters derived using regional records are 1-12 km range and mostly < 8 km (Fig 5, i-l). Hence, the resolved horizontal spread of seismicity in and between the swarms compares well against the global teleseismic data and the locations derived from hydrophone arrays. Although the results shown here are not as accurate as the OBS results, the methods offer the potential advantages of longer observation duration and practicality.

Hypocenters are effectively not resolved in global catalogs to a necessary resolution for studies regarding faulting at mid-ocean ridges. Hypocenters resolved using OBS records have uncertainties of 1-2 km (Figure 12), which allow deeper detachment fault movements to be distinguished from fault movements in the shallower crust (Parnell-Turner et al., 2017; 2020). Craig and Parnell-Turner (2017) noted a lack of seismicity in their experiment in the shallow crust and speculated that this might arise if the fault there was locked, implying that, longer-term, large events occur in the shallow crust. Depth estimates are needed to see if this applies more generally. Modeling long-period seismograms can provide depth estimates, though usually with uncertainties still greater than 1-2 km (Bergman and Solomon, 1984; Huang et al., 1986). Although depth uncertainties arising from our method (~2-4 km; Figure 12) are greater and our methods do not resolve individual deep events well, repeating the exercise for many events could resolve whether seismicity is systematically deep at locations where detachment faults appear to be active from sonar data (i.e., resolve whether the means of the depth distributions vary systematically). This analysis could be carried out by studying seismicity at MOR locations for longer durations or by studying seismicity from many locations.

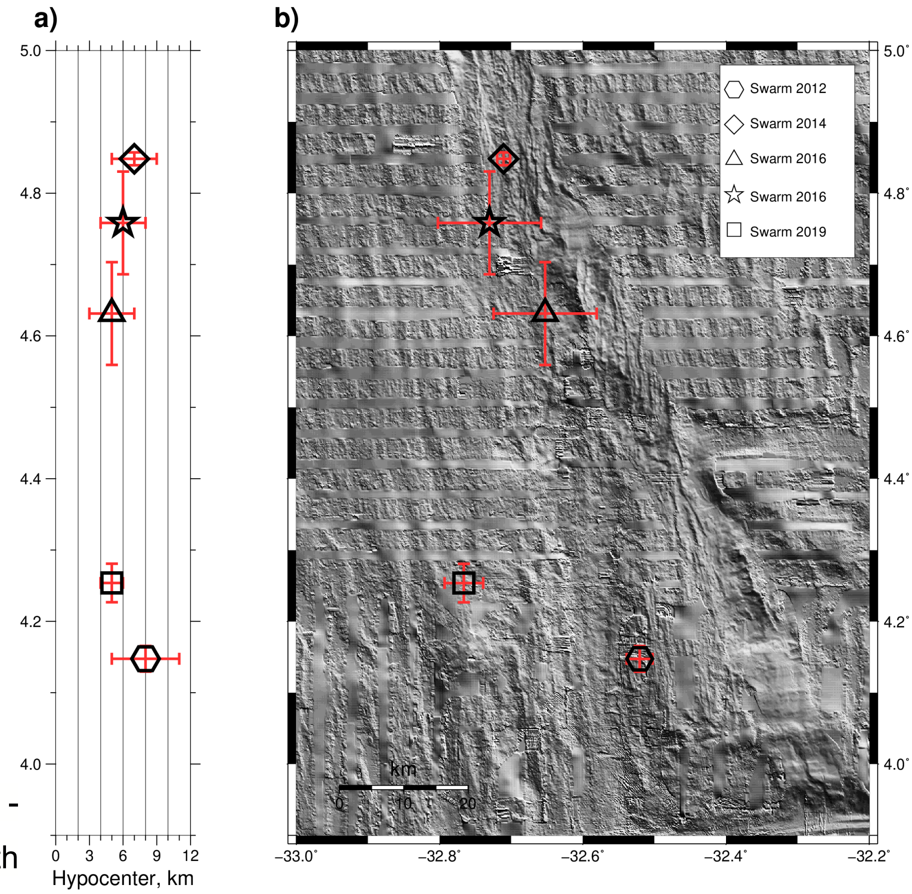

Figure 12 - (a) Depth versus latitude for the strongest earthquakes with Mw>5.4 of each swarm. (b) Those events located on the bathymetry map.

7.0. Conclusion

From our analysis of four earthquake swarms along the Mid-Atlantic Ridge axis at 4-5ºN:

1. The spatial extents of epicenters of four swarm have been resolved using data from broad-band seismic stations located at regional distances. The depths of their largest events were determined using waveform modeling and wpP-P travel time constraints, with the deepest event (2012, Mw 5.5) lying at 8±3 km below the seabed.

2. Because their epicenters did not progress systematically along-axis, the swarms studied appear to be tectonic rather than volcanic. The 2016 results imply coincident activity on many minor faults in the inner floor of the median valley across a region that is ~25 km east-west and ~35 km north-south. Some activity of 2012 may be associated with a detachment fault east of the median valley, although considering the 3 km uncertainties, the 8 km depth of the largest event also overlaps with shallow seismicity of expected more steeply dipping faults.

3. The maximum depths of these swarms are similar to those of seismicity in other parts of the Mid-Atlantic Ridge recorded with OBSs, when considered with associated cross-axis relief. Although earthquake depths were not resolved in our study well enough to address whether the southerly megamullion was active, our methods could be used in the future to study whether seismicity in parts of the ridges is systematically deeper, e.g., where megamullions appear in bathymetry data. In such an approach, many such analyses could be carried out so that the uncertainties of average maximum depth are reduced simply by averaging.

Acknowledgments

We thank the scientists and crews of RVs *Strakhov* and *Atlantis* for collecting the multibeam echo-sounder data presented here. GWSdM is grateful to Bruno Faria for providing the waveform data of the non-public Cape Verdes stations. GWSdM is thankful to Marcelo Assumpção for explaining and beneficial information during the preparation of the manuscript. We also thank Sergey Sokolov and Thomas Funck for very useful information during the preparation of the manuscript. FD is grateful Petrobras (grants 00159-0/2017). AFdN thanks the Brazilian Navy and CNPq (grants 484441/2012-4 and 306813/2017-3) for the support of installing and maintaining the broad-band ASPSP station. AFdN also thank Petrobras and the Brazilian Geological Survey for the support given to the RSBR. We used the Generic Mapping Tools (Wessel et al., 2013) to plot maps, graphics and waveforms. We are grateful to the editor Ramon Carbonell and two anonymous reviewers for their constructive reviews and suggestions that significantly improved this manuscript.

Data availability

Most seismic data are available in the data repository at www.iris.edu and www.rsbr.gov.br. ASPSP station data queries can be addressed to AFdN. Gravity anomaly data were obtained from the International Gravimetric Bureau at http://bgi.obs-mip.fr. The multibeam data were obtained from the National Centers for Environmental Information (www.ncei.noaa.gov).

References

Assumpção, M. (1998). Seismicity and stresses in the Brazilian passive margin. *Bulletin of the Seismological Society of America*, *88*(1), 160-169.

Assumpção, M., Dourado, J. C., Ribotta, L. C., Mohriak, W. U., Dias, F. L., & Barbosa, J. R. (2011). The São Vicente earthquake of 2008 April and seismicity in the continental shelf off SE Brazil: further evidence for flexural stresses. *Geophysical Journal International*, *187*(3), 1076-1088. https://doi.org/10.1111/j.1365-246X.2011.05198.x

Balmino, G., Vales, N., Bonvalot, S., & Briais, A. (2012). Spherical harmonic modelling to ultra-high degree of Bouguer and isostatic anomalies. Journal of Geodesy, 86(7), 499-520. https://doi.org/10.1007/s00190-011-0533-4

Bergman, E. A., & Solomon, S. C. (1984). Source mechanisms of earthquakes near mid-ocean ridges from body waveform inversion: Implications for the early evolution of oceanic lithosphere. *Journal of Geophysical Research: Solid Earth*, *89*(B13), 11415-11441. https://doi.org/10.1029/JB089iB13p11415

Bergman, E. A., & Solomon, S. C. (1990). Earthquake swarms on the Mid-Atlantic Ridge: Products of magmatism or extensional tectonics?. *Journal of Geophysical Research: Solid Earth*, *95*(B4), 4943-4965. https://doi.org/10.1029/JB095iB04p04943

Bianchi, M. B., Assumpção, M., Rocha, M. P., Carvalho, J. M., Azevedo, P. A., Fontes, S. L., ... & Costa, I. S. (2018). The Brazilian seismographic network (RSBR): improving seismic monitoring in Brazil. *Seismological Research Letters*, 89(2A), 452-457. https://doi.org/10.1785/0220170227

Blackman, D. K., Cann, J. R., Janssen, B., & Smith, D. K. (1998). Origin of extensional core complexes: Evidence from the Mid‐Atlantic Ridge at Atlantis fracture zone. *Journal of Geophysical Research: Solid Earth*, *103*(B9), 21315-21333. https://doi.org/10.1029/98JB01756

Blackman D. K, Karner GD, Searle RC (2008) Three-dimensional structure of oceanic core complexes: Effects on gravity signature and ridge flank morphology, Mid-Atlantic Ridge, 30°N. Geochem. Geophys. Geosys. https://doi.org/10.1029/2008GC001951

Bonvalot, S., Balmino, G., Briais, A., M. Kuhn, Peyrefitte, A., Vales N., Biancale, R., Gabalda, G., Reinquin, F., Sarrailh, M. (2012) World Gravity Map. Commission for the Geological Map of the World. Eds. BGI-CGMW-CNES-IRD, Paris

Bratt, S. R., Bergman, E. A., & Solomon, S. C. (1985). Thermoelastic stress: How important as a cause of earthquakes in young oceanic lithosphere?. *Journal of Geophysical Research: Solid Earth*, 90(B12), 10249-10260. https://doi.org/10.1029/JB090iB12p10249

Bull, J. M., & Scrutton, R. A. (1990). Fault reactivation in the central Indian Ocean and the rheology of oceanic lithosphere. *Nature*, *344*(6269), 855-858. https://doi.org/10.1038/344855a0

Canales, J. P., Tucholke, B. E., & Collins, J. A. (2004). Seismic reflection imaging of an oceanic detachment fault: Atlantis megamullion (Mid-Atlantic Ridge, 30 10′ N). *Earth and Planetary Science Letters*, 222(2), 543-560. https://doi.org/10.1016/j.epsl.2004.02.023

Cann, J. R., Blachman, D. K., Smith, D. K., McAllister, E., Janssen, B., Mello, S., Avgerinos, E., Pascoe, A. R., and Escartin, J., 1997, Corrugated slip surfaces formed at ridge-transform intersections on the Mid-Atlantic Ridge: *Nature*, v. 385, p. 329-332. https://doi.org/10.1038/385329a0

Castro, R. R., Stock, J. M., Hauksson, E., & Clayton, R. W. (2017). Active tectonics in the Gulf of California and seismicity (M> 3.0) for the period 2002–2014. *Tectonophysics*, *719*, 4-16.https://doi.org/10.1016/j.tecto.2017.02.015

Cleveland, K. M., Ammon, C. J., & Kintner, J. (2018). Relocation of Light and Moderate-Magnitude (M4–6) Seismicity Along the Central Mid-Atlantic. *Geochemistry, Geophysics, Geosystems*, *19*(8), 2843-2856. https://doi.org/10.1029/2018GC007573

Coutant, O. (1989). Program of numerical simulation AXITRA. Res. Rep. LGIT (in French), Universite Joseph Fourier, Grenoble.

Cowie, P. A. (1998). Normal fault growth in three dimensions in continental and oceanic crust. *GEOPHYSICAL MONOGRAPH-AMERICAN GEOPHYSICAL UNION*, *106*, 325-348.

Craig, T. J., & Parnell-Turner, R. (2017). Depth-varying seismogenesis on an oceanic detachment fault at 13° 20′ N on the Mid-Atlantic Ridge. *Earth and Planetary Science Letters*, *479*, 60-70. https://doi.org/10.1016/j.epsl.2017.09.020

de Melo, G. W., & Do Nascimento, A. F. (2018). Earthquake magnitude relationships for the Saint Peter and Saint Paul archipelago, equatorial atlantic. *Pure and Applied Geophysics*, *175*(3), 741-756. https://doi.org/10.1007/s00024-017-1732-6

de Melo, G. W., Parnell-Turner, R., Dziak, R. P., Smith, D. K., Maia, M., do Nascimento, A. F., & Royer, J. Y. (2020). Uppermost Mantle Velocity beneath the Mid-Atlantic Ridge and Transform Faults in the Equatorial Atlantic Ocean. Bulletin of the Seismological Society of America. https://doi.org/10.1785/0120200248

Dias, F., Zahradník, J., & Assumpção, M. (2016). Path-specific, dispersion-based velocity models and moment tensors of moderate events recorded at few distant stations: Examples from Brazil and Greece. *Journal of South American Earth Sciences*, 71, 344-358. https://doi.org/10.1016/j.jsames.2016.07.004

Dziak, R. P., Fox, C. G., & Schreiner, A. E. (1995). The June-July 1993 seismo-acoustic event at CoAxial segment, Juan de Fuca Ridge: Evidence for a lateral dike injection. *Geophysical Research Letters*, *22*(2), 135-138. https://doi.org/10.1029/94GL01857

Dziak, R. P., & Fox, C. G. (1999). The January 1998 earthquake swarm at Axial Volcano, Juan de Fuca Ridge: Hydroacoustic evidence of seafloor volcanic activity. *Geophysical Research Letters*, *26*(23), 3429-3432. https://doi.org/10.1029/1999GL002332

Dziewonski, A. M., Chou, T. A., & Woodhouse, J. H. (1981). Determination of earthquake source parameters from waveform data for studies of global and regional seismicity. *Journal of Geophysical Research: Solid Earth*, 86(B4), 2825-2852. https://doi.org/10.1029/JB086iB04p02825

Einarsson, P., & Brandsdóttir, B. (1980). Seismological evidence for lateral magma intrusion during the July 1978 deflation of the Krafla volcano in NE-Iceland. *Journal of Geophysics| IF 32.18*, *47*(1), 160-165.

Einarsson, P. (1991). Earthquakes and present-day tectonism in Iceland: *Tectonophysics*, v. 189, p. 261-279. https://doi.org/10.1016/0040-1951(91)90501-I

Ekström, G., Nettles, M., & Dziewoński, A. M. (2012). The global CMT project 2004–2010: Centroid-moment tensors for 13,017 earthquakes. *Physics of the Earth and Planetary Interiors*, 200, 1-9. https://doi.org/10.1016/j.pepi.2012.04.002

Engeln, J. F., Wiens, D. A., & Stein, S. (1986). Mechanisms and depths of Atlantic transform earthquakes. *Journal of Geophysical Research: Solid Earth*, *91*(B1), 548-577. https://doi.org/10.1029/JB091iB01p00548

Escartín, J., & Lin, J. (1995). Ridge offsets, normal faulting, and gravity anomalies of slow spreading ridges. *Journal of Geophysical Research: Solid Earth*, *100*(B4), 6163-6177. https://doi.org/10.1029/94JB03267

Escartín, J., Mével, C., MacLeod, C. J., & McCaig, A. M. (2003). Constraints on deformation conditions and the origin of oceanic detachments: The Mid-Atlantic Ridge core complex at 15 45′ N. *Geochemistry, Geophysics, Geosystems*, *4*(8). https://doi.org/10.1029/2002GC000472

Escartín J, Smith DK, Cann J, Schouten H, Langmuir CH, Escrig S (2008) Central roleof detachment faults in accretion of slow-spreading oceanic lithosphere. *Nature,* 455:790-794. https://doi.org/10.1038/nature07333

Escartín, J., Mevel, C., Petersen, S., Bonnemains, D., Cannat, M., Andreani, M., ... & Garcia, R. (2017). Tectonic structure, evolution, and the nature of oceanic core complexes and their detachment fault zones (13 20′ N and 13 30′ N, Mid Atlantic Ridge). *Geochemistry, Geophysics, Geosystems*, *18*(4), 1451-1482. https://doi.org/10.1002/2016GC006775

Faria, B., & Fonseca, J. F. B. D. (2014). Investigating volcanic hazard in Cape Verde Islands through geophysical monitoring: network description and first results. *Natural Hazards and Earth System Sciences*, 14(2), 485. https://doi.org/10.5194/nhess-14-485-2014

Fox, C. G., Matsumoto, H., & Lau, T. K. A. (2001). Monitoring Pacific Ocean seismicity from an autonomous hydrophone array. *Journal of Geophysical Research: Solid Earth*, *106*(B3), 4183-4206. https://doi.org/10.1029/2000JB900404

GEBCO Compilation Group (2020) GEBCO 2020 Grid. https://doi.org/10.5285/a29c5465-b138-234d-e053-6c86abc040b9.

Giusti, M., Perrot, J., Dziak, R. P., Sukhovich, A., & Maia, M. (2018). The August 2010 earthquake swarm at North FAMOUS–FAMOUS segments, Mid-Atlantic Ridge: geophysical evidence of dike intrusion. *Geophysical Journal International*, *215*(1), 181-195. https://doi.org/10.1093/gji/ggy239

Goslin, J., Lourenço, N., Dziak, R. P., Bohnenstiehl, D. R., Haxel, J., & Luis, J. (2005). Long-term seismicity of the Reykjanes Ridge (North Atlantic) recorded by a regional hydrophone array. *Geophysical Journal International*, *162*(2), 516-524. https://doi.org/10.1111/j.1365-246X.2005.02678.x

Goslin, J., Perrot, J., Royer, J. Y., Martin, C., Lourenço, N., Luis, J., ... & Bazin, S. (2012). Spatiotemporal distribution of the seismicity along the Mid-Atlantic Ridge north of the Azores from hydroacoustic data: Insights into seismogenic processes in a ridge–hot spot context. *Geochemistry, Geophysics, Geosystems*, *13*(2).

Grevemeyer, I., Reston, T. J., & Moeller, S. (2013). Microseismicity of the Mid-Atlantic Ridge at 7° S–8° 15′ S and at the Logatchev Massif oceanic core complex at 14° 40′ N–14° 50′ N. *Geochemistry, Geophysics, Geosystems*, 14(9), 3532-3554. https://doi.org/10.1002/ggge.20197

Hanka, W., Saul, J., Weber, B., Becker, J., Harjadi, P., Rudloff, A., ... & Clinton, J. (2010). Real-time earthquake monitoring for tsunami warning in the Indian Ocean and beyond. Natural Hazards & Earth System Sciences, 10(12). https://doi.org/10.5194/nhess-10-2611-2010

Hooft, E. E. E., Detrick, R. S., Toomey, D. R., Collins, J. A., & Lin, J. (2000). Crustal thickness and structure along three contrasting spreading segments of the Mid-Atlantic Ridge, 33.5–35 N. *Journal of Geophysical Research: Solid Earth*, 105(B4), 8205-8226. https://doi.org/10.1029/1999JB900442

Huang, P. Y., Solomon, S. C., Bergman, E. A., & Nabelek, J. L. (1986). Focal depths and mechanism of Mid-Atlantic Ridge earthquakes from body waveform inversion. *Journal of Geophysical Research: Solid Earth*, 91(B1), 579-598. https://doi.org/10.1029/JB091iB01p00579

Kennett, B. L. N., & Engdahl, E. R. (1991). Traveltimes for global earthquake location and phase identification. *Geophysical Journal International*, 105(2), 429-465. https://doi.org/10.1111/j.1365-246X.1991.tb06724.x

Klein, F. W., Einarsson, P., & Wyss, M. (1977). The Reykjanes Peninsula, Iceland, earthquake swarm of September 1972 and its tectonic significance. *Journal of Geophysical Research*, *82*(5), 865-888. https://doi.org/10.1029/JB082i005p00865

Laske, G., Masters, G., Ma, Z., & Pasyanos, M. (2013, April). Update on CRUST1. 0—A 1-degree global model of Earth's crust. In Geophys. Res. Abstr (Vol. 15, p. 2658). Vienna, Austria: EGU General Assembly.

Lee, W. H. K., & Valdes, C. M. (1985). HYPO71PC: A personal computer version of the HYPO71 earthquake location program (Vol. 85, No. 749). US Geological Survey.

Macdonald, K. C., and Luyendyk, B. P. (1977). Deep-tow studies of the structure of the Mid-Atlantic Ridge crest near latitude 37° N. *Geol. Soc. Am. Bull.*, v. 88, p. 621-636. https://doi.org/10.1130/0016-7606(1977)88<621:DSOTSO>2.0.CO;2

Olive, J.-A., and Escartín, J. (2016. Dependence of seismic coupling on normal fault style along the Northern Mid-Atlantic Ridge. *Geochemistry, Geophysics, Geosystems*, v. 17, p. 4128-4152. https://doi.org/10.1002/2016GC006460

Parnell-Turner, R., Palmiotto, C., Zheleznov, A., Smith, D., Fowler, M., Bonnemains, D., ... & Dziak, B. (2012). Seismicity of the Equatorial Mid-Atlantic Ridge and its Large Offset Transforms. InterRidge News, 21, 24-27.

Parnell-Turner, R., Sohn, R. A., Peirce, C., Reston, T. J., MacLeod, C. J., Searle, R. C., & Simão, N. M. (2017). Oceanic detachment faults generate compression in extension. *Geology*, *45*(10), 923-926. https://doi.org/10.1130/G39232.1

Parnell-Turner, R., Sohn, R. A., Peirce, C., Reston, T. J., MacLeod, C. J., Searle, R. C., & Simão, N. M. (2020). Seismicity trends and detachment fault structure at 13° N, Mid-Atlantic Ridge. *Geology*. https://doi.org/10.1130/G48420.1

Pérez-Díaz, L., & Eagles, G. (2017). South Atlantic paleobathymetry since early Cretaceous. *Scientific reports*, *7*(1), 1-16. https://doi.org/10.1038/s41598-017-11959-7

Romanowicz, B., Cara, M., Fel, J. F., & Rouland, D. (1984). GEOSCOPE: A French initiative in long-period three-component global seismic networks. *Eos*, Transactions American Geophysical Union, 65(42), 753-753. https://doi.org/10.1029/EO065i042p00753-01

Ryan, W. B., Carbotte, S. M., Coplan, J. O., O'Hara, S., Melkonian, A., Arko, R., ... & Zemsky, R. (2009). Global multi-resolution topography synthesis. *Geochemistry, Geophysics, Geosystems*, *10*(3).

Scripps Institution of Oceanography. (1986). IRIS/IDA Seismic Network. International Federation of Digital Seismograph Networks. https://doi.org/10.7914/SN/II

Searle RC, Cowie PA, Mitchell NC, Allerton S, MacLeod CJ, Escartin J, Russell SM, Slootweg PA, Tanaka T. (1998). Fault structure and detailed evolution of a slow spreading ridge segment: the Mid-Atlantic Ridge at 29˚N. *Earth Planet. Sci. Lett*. 154:167-183. https://doi.org/10.1016/S0012-821X(97)00160-X

Shaw, P. R., and Lin, J. (1993) Causes and consequences of variations in faulting style at a Mid-Atlantic Ridge. *J. Geophys. Res*., v. 98, p. 21839-21851. https://doi.org/10.1029/93JB01565

Shaw, P. S. (1992) Ridge segmentation, faulting and crustal thickness in the Atlantic Ocean: Nature, v. 358, p. 490-493. https://doi.org/10.1038/358490a0

Shearer, P. M., & Orcutt, J. A. (1987). Surface and near-surface effects on seismic waves—theory and borehole seismometer results. *Bulletin of the Seismological Society of America*, *77*(4), 1168-1196.

Scholz, C. H., 2002, The mechanics of earthquakes and faulting, New York, Cambridge University Press, 471 p.

Simao, N., Escartin, J., Goslin, J., Haxel, J., Cannat, M., & Dziak, R. (2010). Regional seismicity of the Mid-Atlantic Ridge: observations from autonomous hydrophone arrays. *Geophysical Journal International*, *183*(3), 1559-1578. https://doi.org/10.1111/j.1365-246X.2010.04815.x

Smith, D. K., Tolstoy, M., Fox, C. G., Bohnenstiehl, D. R., Matsumoto, H., & J. Fowler, M. (2002). Hydroacoustic monitoring of seismicity at the slow-spreading Mid-Atlantic Ridge. *Geophysical Research Letters*, *29*(11), 13-1. https://doi.org/10.1029/2001GL013912

Smith, D. K., Escartin, J., Cannat, M., Tolstoy, M., Fox, C. G., Bohnenstiehl, D. R., & Bazin, S. (2003). Spatial and temporal distribution of seismicity along the northern Mid-Atlantic Ridge (15°–35° N). *Journal of Geophysical Research: Solid Earth*, *108*(B3). https://doi.org/10.1029/2002JB001964

Smith, D. K., Cann, J. R., & Escartín, J. (2006). Widespread active detachment faulting and core complex formation near 13 N on the Mid-Atlantic Ridge. *Nature*, *442*(7101), 440-443. https://doi.org/10.1038/nature04950

Smith, D. K., Escartín, J., Schouten, H., & Cann, J. R. (2008). Fault rotation and core complex formation: Significant processes in seafloor formation at slow-spreading mid-ocean ridges (Mid-Atlantic Ridge, 13–15 N). *Geochemistry, Geophysics, Geosystems*, *9*(3). (https://doi.org/10.1029/2007GC001699)

Smith, D. K et al. (2012a). AT21-03 cruise, RV Atlantis, https://www.ngdc.noaa.gov/

Smith, D. K., R. P. Dziak, C. Palmiotto, R. Parnell-Turner, and A. Zheleznov (2012b). The seismicity of the equatorial Mid-Atlantic Ridge and its long-offset transforms, Presented at the 2012 AGU Fall Meeting, San Francisco, California, 5-9 December, Abstract OS13B-1720.

Sokos, E. N., & Zahradnik, J. (2008). ISOLA a Fortran code and a Matlab GUI to perform multiple-point source inversion of seismic data. *Computers & Geosciences*, 34(8), 967-977. https://doi.org/10.1016/j.cageo.2007.07.005

Sokos, E., & Zahradník, J. (2013). Evaluating centroid-moment-tensor uncertainty in the new version of ISOLA software. *Seismological Research Letters*, 84(4), 656-665. https://doi.org/10.1785/0220130002

Solomon, S. C., Huang, P. Y., and Meinke, L. (1988) The seismic moment budget of slowly spreading ridges. *Nature*, v. 334, p. 58-60. https://doi.org/10.1038/334058a0

Sykes, L. R. (1967) Mechanism of earthquakes and nature of faulting on mid-ocean ridges. *J. Geophys. Res.*, v. 72, p. 2131-2153. https://doi.org/10.1029/JZ072i008p02131

Tapponnier, P., & Francheteau, J. (1978). Necking of the lithosphere and the mechanics of slowly accreting plate boundaries. *Journal of Geophysical Research: Solid Earth*, *83*(B8), 3955-3970.

Thatcher, W., and Hill, D. P. (1995). A simple model for the fault-generated morphology of slow-spreading mid-ocean ridges. *J. Geophys. Res.*, v. 100, p. 561-570. https://doi.org/10.1029/94JB02593

Toomey, D. R., Solomon, S. C., Purdy, G. M., & Murray, M. H. (1985). Microearthquakes beneath the median valley of the Mid-Atlantic Ridge near 23° N: Hypocenters and focal mechanisms. *Journal of Geophysical Research: Solid Earth*, 90(B7), 5443-5458. https://doi.org/10.1029/JB090iB07p05443

Toomey, D. R., Solomon, S. C., & Purdy, G. M. (1988). Microearthquakes beneath median valley of Mid-Atlantic Ridge near 23° N: Tomography and tectonics. *Journal of Geophysical Research: Solid Earth*, 93(B8), 9093-9112. https://doi.org/10.1029/JB093iB08p09093

Tucholke, B. E., Behn, M. D., Buck, W. R., & Lin, J. (2008). Role of melt supply in oceanic detachment faulting and formation of megamullions. *Geology*, 36(6), 455-458. https://doi.org/10.1130/G24639A.1

Udintsev, G. B., Beresnev, A. F., Golod, V. M., Kol'tsova, A. V., Kurentsova, N. A., Zakharov, M. V., ... & Udintsev, V. G. (1995). Geological structure of the Strakhov fracture zone (equatorial segment of the Mid-Atlantic ridge). *Oceanology of the Russian Academy of Sciences*, 35(4), 544-558.

Udintsev GB, Hall JK, Udintsev VG, Knjazev AB (1996) Topography of the Equatorial segment of the Mid-Atlantic Ridge after multibeam echosounding. In: Udintsev GB(ed) Equatorial Segment of the Mid-Atlantic Ridge, Intergovernmental Oceanographic Commission technical series No. 46. UNESCO, Paris, France, pp8-14.

Vogt, P. R., & Jung, W. Y. (2004). The Terceira Rift as hyper-slow, hotspot-dominated oblique spreading axis: a comparison with other slow-spreading plate boundaries. *Earth and Planetary*

Science Letters, *218*(1-2), 77-90. https://doi.org/10.1016/S0012-821X(03)00627-7

Wolfe, C. J., Bergman, E. A., & Solomon, S. C. (1993). Oceanic transform earthquakes with unusual mechanisms or locations: Relation to fault geometry and state of stress in the adjacent lithosphere. *Journal of Geophysical Research: Solid Earth*, *98*(B9), 16187-16211. https://doi.org/10.1029/93JB00887

Wright, T. J., Ebinger, C., Biggs, J., Ayele, A., Yirgu, G., Keir, D., & Stork, A. (2006). Magma-maintained rift segmentation at continental rupture in the 2005 Afar dyking episode. *Nature*, *442*(7100), 291-294.https://doi.org/10.1038/nature04978

Zahradník, J., & Sokos, E. (2018). ISOLA code for multiple-point source modeling. In Moment Tensor Solutions (pp. 1-28). Springer, Cham. https://doi.org/10.1007/978-3-319-77359-9_1